

Article

Elastocaloric and Magnetocaloric Effects Linked to the Martensitic Transformation in Bulk Ni₅₅Fe₁₁Mn₇Ga₂₇ Alloys Produced by Arc Melting and Spark Plasma Sintering

J. D. Navarro-García ^{1,*} , J. P. Camarillo-García ² , F. Alvarado-Hernández ², J. L. Sánchez Llamazares ^{1,*}  and H. Flores-Zúñiga ¹

¹ Instituto Potosino de Investigación Científica y Tecnológica A.C., Camino a la Presa San José 2055, Col. Lomas 4 Section, San Luis Potosí 78216, Mexico; horacio.flores@ipicyt.edu.mx

² Unidad Académica de Ingeniería I, Universidad Autónoma de Zacatecas, Ramón López Velarde 801, Col. Centro, Zacatecas 98000, Mexico; jp.camarillo.garcia@uaz.edu.mx or jp.camarillo.garcia@gmail.com (J.P.C.-G.); ingenierofah@gmail.com (F.A.-H.)

* Correspondence: daniel.navarro@ipicyt.edu.mx (J.D.N.-G.); jose.sanchez@ipicyt.edu.mx (J.L.S.L.); Tel.: +52-444-8342000 (J.L.S.L.)



Citation: Navarro-García, J.D.; Camarillo-García, J.P.; Alvarado-Hernández, F.; Sánchez Llamazares, J.L.; Flores-Zúñiga, H. Elastocaloric and Magnetocaloric Effects Linked to the Martensitic Transformation in Bulk Ni₅₅Fe₁₁Mn₇Ga₂₇ Alloys Produced by Arc Melting and Spark Plasma Sintering. *Metals* **2022**, *12*, 273. <https://doi.org/10.3390/met12020273>

Academic Editor: Alexander V. Shelyakov

Received: 24 December 2021

Accepted: 27 January 2022

Published: 2 February 2022

Publisher's Note: MDPI stays neutral with regard to jurisdictional claims in published maps and institutional affiliations.



Copyright: © 2022 by the authors. Licensee MDPI, Basel, Switzerland. This article is an open access article distributed under the terms and conditions of the Creative Commons Attribution (CC BY) license (<https://creativecommons.org/licenses/by/4.0/>).

Abstract: The investigation of caloric effects linked to first-order structural transitions in Heusler-type alloys has become a subject of considerable current interest due to their potential utilization as refrigerants in solid-state cooling devices. This study is mainly motivated by the possibility of developing refrigeration devices of improved energy efficiency with a reduced environmental impact. We produced partially textured and isotropic bulk samples of the Heusler-type magnetic shape memory alloy Ni₅₅Fe₁₁Mn₇Ga₂₇ by arc melting and spark plasma sintering (SPS), respectively. Their structural, microstructural, and phase transition characteristics and magnetocaloric and elastocaloric effects, associated with first-order martensitic transformation (MT), were studied. The elemental chemical compositions of both samples were close to nominal, and a martensitic-like structural transformation appeared around room temperature with similar starting and finishing structural transition temperatures. At room temperature, austenite exhibited a highly ordered L2₁-type crystal structure. The partial grain orientation and isotropic nature of the arc-melted and SPS samples, respectively, were revealed by X-ray diffraction and SEM observations of the microstructure. For the arc-melted sample, austenite grains preferentially grew in the (100) direction parallel to the thermal gradient during solidification. The favorable effect of the texture on the elastocaloric response was demonstrated. Finally, due to its partial grain orientation, the arc-melted bulk sample showed superior values of maximum magnetic entropy change ($|\Delta S_M|^{\max} = 18.6 \text{ Jkg}^{-1}\text{K}^{-1}$ at 5 T) and elastocaloric adiabatic temperature change ($|\Delta T_{\text{ad}}^{\text{me}}|^{\max} = 2.4 \text{ K}$ at 120 MPa) to those measured for the SPS sample ($|\Delta S_M|^{\max} = 8.5 \text{ Jkg}^{-1}\text{K}^{-1}$ and $|\Delta T_{\text{ad}}^{\text{me}}|^{\max} = 0.8 \text{ K}$).

Keywords: Ni-Fe-Ga magnetic shape memory alloys; elastocaloric and magnetocaloric effects; martensitic transformation; spark plasma sintering

1. Introduction

The recent interest in the development of solid-state refrigeration devices as a more efficient alternative to conventional gas compression refrigeration has encouraged the investigation of the caloric effects linked to first-order phase transitions in different families of solids [1]. Among them, (Ni,Mn)-based Heusler-type alloys undergoing a diffusion-less martensitic transformation (MT) have been the subject of considerable interest due to their multifunctional nature [1]. Elastocaloric (eC) and magnetocaloric (MC) effects are thermal responses to external stimuli, mechanical or magnetic, respectively, characterized by the adiabatic temperature change ΔT_{ad} or the isothermal entropy change ΔS due to the application of a change in the stress $\Delta\sigma$ or the magnetic field $\mu_0\Delta H$ [2]. Martensitic

transformation (MT) in shape memory alloys (SMAs) may show a high sensitivity to the application of external uniaxial stress, which, in some cases, gives rise to a large eC effect, making them promising materials for the development of solid-state refrigeration devices [3–5]. However, depending on the alloy, a large load may be needed to induce the structural transformation compromising the potential applicability [6]. In magnetic shape memory alloys (MSMA), the structural change is accompanied by a change in the magnetic state of the martensite and austenite phases with the consequent magnetization change ΔM , which in turn may lead to a large MC effect [7]. Thus, the material is considered multicaloric if different caloric effects linked to the transition can be driven simultaneously, or sequentially, by the application of more than one external field or stimulus. Currently, there is a rising interest in the investigation of multicaloric materials [8].

(Ni, Mn)-based Heusler-type magnetic shape memory alloys have received particular attention due to their multicaloric capability [9]. The present work focuses on an MSMA derived from a $\text{Ni}_{55}\text{Fe}_{19}\text{Ga}_{26}$ alloy in which the Fe was partially substituted by Mn. For properly chosen compositions, MT in Ni-Fe-Ga alloys appears around room temperature (RT) [1,10]. The structural transition on cooling is from a cubic ferromagnetic austenite with a B2-type or the $L2_1$ -type crystal structure, depending on the thermal treatment received above 973 K [11], to 10M or 14M modulated ferromagnetic martensite [10–13]. The two factors that motivated the present investigation were the good mechanical properties of this alloy system in comparison to other (Ni,Mn)-based alloys (which are further improved with the precipitation of the so-called γ phase [14]) and the evidence that the partial replacement of Fe by Mn increases the entropy of the MT without significantly modifying the MT temperatures or the γ low concentration present in the $\text{Ni}_{55}\text{Fe}_{19}\text{Ga}_{26}$ composition [15]. Moreover, Ni-Fe-Ga alloys can be easily obtained by a conventional melting technique, such as arc melting, followed by the thermal treatment required in order to produce the desired austenitic structure [16]. Another aspect addressed in this work was the consolidation of these alloys by spark plasma sintering (SPS). This pressure-assisted processing technique allows the fabrication of highly dense shaped pieces of a large variety of metallic and ceramic materials in a very short thermal processing time and at relatively low temperatures in comparison to those reported when conventional sintering is used [17,18]. The ability of the SPS technique to produce highly dense (Ni,Mn)-based alloys with improved mechanical resistance has been highlighted by several authors [18–21] example, in [22], this processing route was used to fabricate Ni-Co-Mn-Sn alloys with similar MT temperatures and magnetic properties to those obtained for the bulk alloy produced by induction melting [22]. To the best of our knowledge, (Ni-Fe-Ga)-based alloys have not yet been produced by SPS.

Although there have been several studies about the magnetic characterization of Ni-Fe-Ga alloys [23–27], the MC effect has rarely been reported, mainly because the maximum magnetic entropy change $|\Delta S_M|^{\max}$ displayed by these alloys does not exceed $\sim 5 \text{ Jkg}^{-1}\text{K}^{-1}$ at $\mu_0\Delta H = 5 \text{ T}$ [15,28], with a single report of $\sim 12 \text{ Jkg}^{-1}\text{K}^{-1}$ [14]. However, eC effect reports on single crystals or textured alloys have recently been presented with large mechanically induced entropy change or adiabatic temperature change [3,14,29]. Therefore, in this investigation, we synthesized polycrystalline samples of the quaternary $\text{Ni}_{55}\text{Fe}_{11}\text{Mn}_7\text{Ga}_{27}$ alloy by arc melting and spark plasma sintering (SPS), and studied their microstructural, structural, magnetocaloric, and elastocaloric properties.

2. Materials and Methods

Arc-melted ingots of nominal composition $\text{Ni}_{55}\text{Fe}_{11}\text{Mn}_7\text{Ga}_{27}$ were synthesized from pure elements ($\geq 99.9\%$); a copper crucible with a flat base was used to promote vertical grain growth along the thermal gradient. Next, the samples were enclosed in quartz capsules in a UHP argon atmosphere to receive two subsequent thermal treatments: homogenization at 1273 K for 24 h and a chemical ordering treatment at 773 K for 1 h (both ending by quenching in iced water). From one of the arc melted samples, which will be referred to hereafter as “bulk”, different specimens were cut with a low-speed diamond saw for the different studies performed. The other was manually pulverized with an agate

mortar to be processed by SPS (i.e., SPS sample). The SPS process was carried out in a Labox-210 SPS system (from Sinter Land Inc., Niigata, Japan), using a 15 mm diameter graphite die, under vacuum at constant pressure of 30 MPa. The time evolution of the vertical displacement and temperature through the SPS process is shown in Figure 1. Notably, the vertical displacement continuously rises to 693 K (420 °C), due to the thermal expansion of the sample, whereas from this temperature and up to 1182 K (909 °C), a continuous shrinkage takes place for 9 min, denoting the occurrence of sintering. The obtained sintered disc showed a density ρ of $8.4 \times 10^3 \text{ kg}\cdot\text{m}^{-3}$; this was ~99% of the maximum expected value [30].

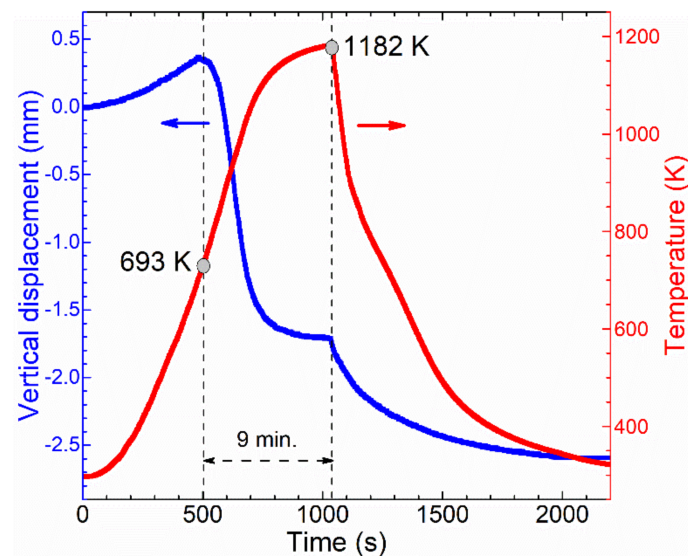


Figure 1. Vertical displacement and temperature versus time along the SPS process.

Differential scanning calorimetry (DSC) curves were measured on a TA-DSC Q200 at a T sweep rate of 10 Kmin^{-1} to determine the enthalpy ΔH_{st} , entropy ΔS_{st} and characteristic starting and finishing temperatures of the structural transformation. Martensitic and reverse martensitic starting and finishing temperatures are referred to as M_S and M_f , and A_S and A_f , respectively; the method for their determination is given below. The X-ray diffraction (XRD) analyses were performed in a Rigaku Smartlab high-resolution powder diffractometer ($\text{Cu-K}\alpha$ radiation). The microstructural characterization was performed using a QUANTA FEG 250 scanning electron microscope (SEM) from FEI; the system was equipped with an EDS system from EDAX. Magnetization as a function of temperature $M(T)$ curves was measured at a temperature sweep rate of 1.0 Kmin^{-1} on parallelepiped-shaped specimens; for the arc-melted and SPS samples, the major axis of the parallelepipeds was parallel to the thermal gradient and pressing directions, respectively. The magnetic field was applied along the greatest length of the samples to minimize the internal demagnetizing field. The measurements were performed using the vibrating sample magnetometer option of a Quantum Design PPMS[®] Dynacool[®] system. Finally, in [2], the purpose-built equipment used for the direct measurement of the eC adiabatic temperature change ΔT_{ad}^{me} is described. This measurement was performed on parallelepiped-shaped specimens cut from the bulk and SPS samples; their physical dimensions were $4.3 \times 2.2 \times 2.1 \text{ mm}^3$ and $2.2 \times 2.3 \times 2.1 \text{ mm}^3$ (i.e., height, width, and length), respectively. As temperature probe, the system used a tiny K-type thermocouple (0.13 mm in diameter). Compressing uniaxial load change of 120 MPa was applied parallel to the thermal gradient during solidification and pressing direction for bulk and SPS samples, respectively.

3. Results and Discussion

Figure 2a shows the heating and cooling DSC curves for both samples. The exothermic and endothermic peaks reveal, respectively, the martensitic and austenitic transitions of

both alloys. By determining the transformed fraction as a function of the temperature of one phase to the other for the structural transition in both directions (i.e., heating and cooling), the start and finish temperatures of the structural transformation were determined at 5% and 95% of the transformation percentage, respectively. Their values, together with the thermal hysteresis of the transformation ΔT_{hyst} (determined as $\Delta T_{\text{hyst}} = A_f - M_s$), are listed in Table 1. Notably, the structural transition in both samples appears around RT and their starting and finishing structural transition temperatures are similar. Table 1 also shows that, within the error of the determination, the averaged elemental chemical composition determined by EDS is similar in both samples and close to nominal. This result is relevant, since the transition temperatures in these (Ni-Fe-Ga)-based alloys are highly sensitive to composition alterations [31]. Consequently, both results highlight the effectiveness of the SPS technique at consolidating (Ni-Fe-Ga)-based alloys.

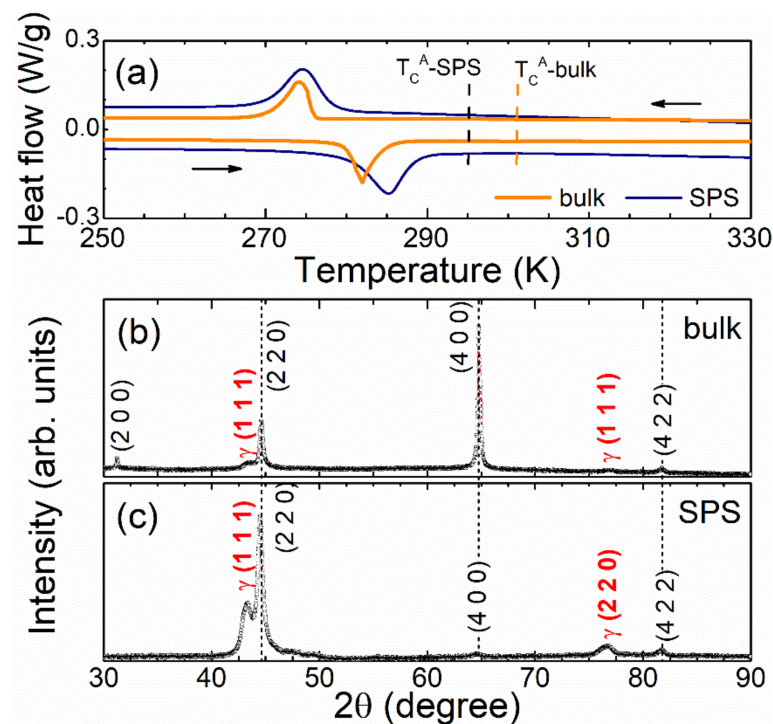


Figure 2. (a) DSC curves for bulk and SPS samples. Vertical dotted lines were drawn to indicate the Curie temperature of austenite for both samples ($T_C^A\text{-bulk}$ and $T_C^A\text{-SPS}$, respectively). (b,c) Indexed XRD patterns for bulk and SPS samples, respectively.

Table 1. Characteristic starting and finishing temperatures, thermal hysteresis, structural enthalpy and entropy of the structural transformation, Curie temperature of austenite (determined from the minimum of the $dM/dT(T)$ curve measured at 5 mT), and experimental elemental chemical composition determined by EDS (at. %) for bulk arc-melted and SPS samples.

Sample	Method	M_s (K)	M_f (K)	A_s (K)	A_f (K)	ΔT_{hyst} (K)	ΔH_{st} (Jg^{-1})	ΔS_{st} ($\text{Jkg}^{-1}\text{K}^{-1}$)	T_C^A (K)	Experimental Composition (at. %)
Bulk	DSC	276	269	277	286	8	5.9	21.3	301	$\text{Ni}_{55.7\pm 0.2}\text{Fe}_{11.9\pm 0.2}\text{Mn}_{7.2\pm 0.1}\text{Ga}_{25.2\pm 0.4}$
	$M(T)^{5\text{mT}}$	276	273	280	282	6	-	-		
SPS	DSC	278	262	279	290	11	5.5	19.1	295	$\text{Ni}_{55.8\pm 0.1}\text{Fe}_{12.0\pm 0.1}\text{Mn}_{6.9\pm 0.1}\text{Ga}_{25.3\pm 0.1}$
	$M(T)^{5\text{mT}}$	276	272	280	286	10	-	-		

The XRD patterns shown in Figure 2b,c were obtained with an X-ray beam impinging on a plane perpendicular to the thermal gradient during the solidification for the bulk arc-melted sample and on the surface of the sintered disc for the SPS sample, respectively. The present phases in the samples were initially identified based on the ICDD PDF cards 04-014-5690 and 01-077-7907 as a cubic austenite with an $L2_1$ crystal structure and lattice

parameter $a = 5.774(7) \text{ \AA}$ (in good agreement with the cooling DSC curves), and a cubic gamma phase with $a = 3.614(7) \text{ \AA}$ [11], respectively. Vertical dashed lines were drawn in Figure 2b,c across both XRD graphs to underline that for both samples, the respective Bragg reflections of austenite appear in the same 2θ position, whereas the additional weak reflections observed in the patterns correspond to the γ phase. To roughly estimate the amount of gamma phase, a piece of the bulk arc-melted sample was finely pulverized to collect its diffraction pattern. In Figure S1 in the Supplementary Material, the Rietveld refinement of this pattern considering the coexistence of these two phases is shown; the refinement was performed using the Powder Cell program, version 2.4. The amount of γ phase was quantified as $\sim 6\%$ vol. Finally, it must be noted that the peak intensities in the XRD pattern for the SPS sample correspond to an isotropic polycrystal, whereas for the bulk arc-melted sample, austenite grains preferentially grow in the (100) direction oriented along the thermal gradient during solidification. In order to obtain further information about the partial preferential and non-preferential grain orientation in the studied samples, the samples were prepared for SEM observations as follows. The bulk and SPS samples were cut parallel to the thermal gradient during solidification and to the pressing direction during the SPS process, respectively, and carefully polished. Their typical microstructures are shown in Figures 3a and 3b, respectively. The former shows coarse column-shaped grains (note the 2 mm magnification scale) whose major growth direction is parallel to the thermal gradient during solidification (schematically represented in the drawing inserted into Figure 3a). By contrast, the microstructure of the SPS sample is formed by smaller polyhedral grains ($< 50 \mu\text{m}$) not showing a preferential orientation relative to the pressing direction (i.e., the shape of the manually crushed powder particles is replicated in the sintered sample). Hence, the respective XRD patterns confirm the preferential grain orientation of the arc-melted sample as well as the isotropic nature of the SPS sample, while the microstructural analysis verifies the characteristic grain morphology of each synthesis method.

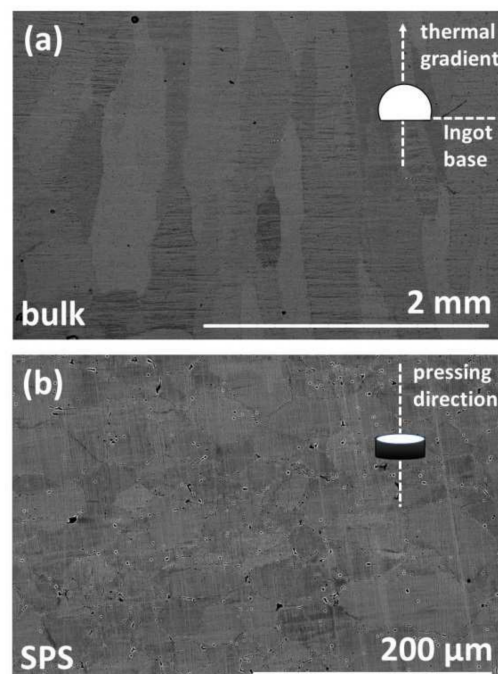


Figure 3. SEM micrographs of the typical microstructure observed for the bulk arc-melted alloy in the plane parallel to thermal gradient (a) and for the SPS sample in the plane parallel to pressing direction during the SPS process (b). The white solid semi-circle and the vertical dashed arrow in (a) schematically represent the cross-sectional view of the arc-melted ingot with its nearly flat bottom surface and the direction of thermal gradient during solidification, respectively. The white vertical dashed line and elliptical area in (b) represent the pressing direction during SPS process and the analyzed plane, correspondingly.

$M(T)$ curves under 5 mT and 5 T following zero-field-cooling (ZFC) and field-cooling (FC) regimens in the structural phase transition region are depicted in Figure 4a,b. From the curves measured at 5 mT, the characteristic structural transition temperatures were also determined by simple extrapolation, whereas the temperature of austenite T_C^A was obtained from the minimum of the $dM/dT(T)$ curves; the results are listed in Table 1. Notably, there is good agreement between the values determined for the structural transition temperatures from the $M(T)^{5\text{mT}}$ curves and the DSC scans; the observable slight 6 K difference in T_C^A was attributed to the different last thermal treatment that they received. Furthermore, a positive shift in the transformation temperatures ($dT_M/d\mu_0H$) of 0.4 K T^{-1} was estimated in both the bulk and SPS samples.

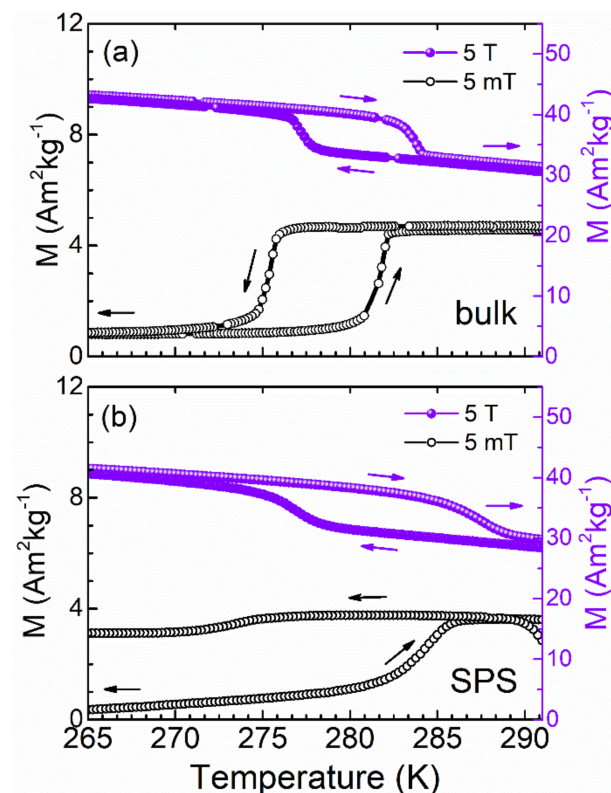


Figure 4. ZFC and FC $M(T)$ curves under 5 mT and 5 T in the temperature range where the structural phase transition occurs for bulk (a) and SPS (b) samples. The horizontal arrows indicate the scale that correspond to the $M(T)$ values measured at 5 mT (left) and 5 T (right), respectively.

The magnetic entropy change as a function of the temperature $\Delta S_M(T)$ curves through direct and inverse MT were estimated from the numerical integration of the Maxwell relation (i.e., $\Delta S_M(T, \mu_0\Delta H) = \mu_0 \int_0^{H_{\max}} \left[\frac{\partial M(T, H')}{\partial T} \right]_{H'} dH'$). The sets of isofield $M(T)$ curves measured for this purpose are depicted in Figure 5a,b,c,d,e; they were measured by always crossing the corresponding phase transition in the same direction (up to a maximum applied magnetic field μ_0H_{\max} of 5 T). The positive shift in the transition underlines the occurrence of a conventional magnetocaloric effect. It must be noted that the magnetization change across the magnetostructural transition is similar in both samples ($\sim 6.5\text{ Am}^2\text{kg}^{-1}$), but the transition is sharp in the arc-melted sample, suggesting a higher $|\Delta S_M|^{\max}$ (due to its direct proportionality to $|dM/dT|$). This also explains the different full width at half-maximum temperature interval δT_{FWHM} of the respective $\Delta S_M(T)$ curves (as shown in Figure 5c,f. Bulk sample exhibits a $|\Delta S_M|^{\max}$ of 18.6 and $14.7\text{ Jkg}^{-1}\text{K}^{-1}$ for direct and inverse MT, respectively, under $\mu_0\Delta H_{\max} = 5\text{ T}$ ($\delta T_{\text{FWHM}} = 2.0$ and 2.2 K). The difference observed in $|\Delta S_M|^{\max}$ between the cooling and heating paths is attributed to the fact that: (i) the formation of austenite and martensite follow different mechanisms and (ii) during

cooling, the thermal range in which the phase induction takes place is smaller. By contrast, the SPS sample displays $|\Delta S_M|^{\max}$ values of 8.5 in both directions ($\delta T_{\text{FWHM}} = 4.0$ and 4.4 K). In this case, the similar $|\Delta S_M|^{\max}$ value obtained for heating and cooling transitions could be related to the smaller average grain size of the sample, which limits the effect of the phase induction mechanisms. However, what seems to be more decisive for this sample is that the thermal range of the transition for both cooling and heating processes is similar. Despite the $|\Delta S_M|^{\max}$ difference, the relative cooling power, RCP, which measures the amount of energy that it is possible to exchange per cooling cycle under ideal conditions, results in 28 Jkg^{-1} at 5 T for both samples. The RCP was obtained by calculating the area below the $|\Delta S_M(T)|$ curves in the temperature interval δT_{FWHM} . It is worth highlighting that despite the moderate values of $|\Delta S_M|^{\max}$ displayed, they exceed the largest values previously reported for the studied alloy system ($|\Delta S_M|^{\max} = 7.5\text{--}12.0 \text{ Jkg}^{-1}\text{K}^{-1}$) [15]. The magnetocaloric parameters for both the direct and reverse MT for both samples are summarized in Table 2.

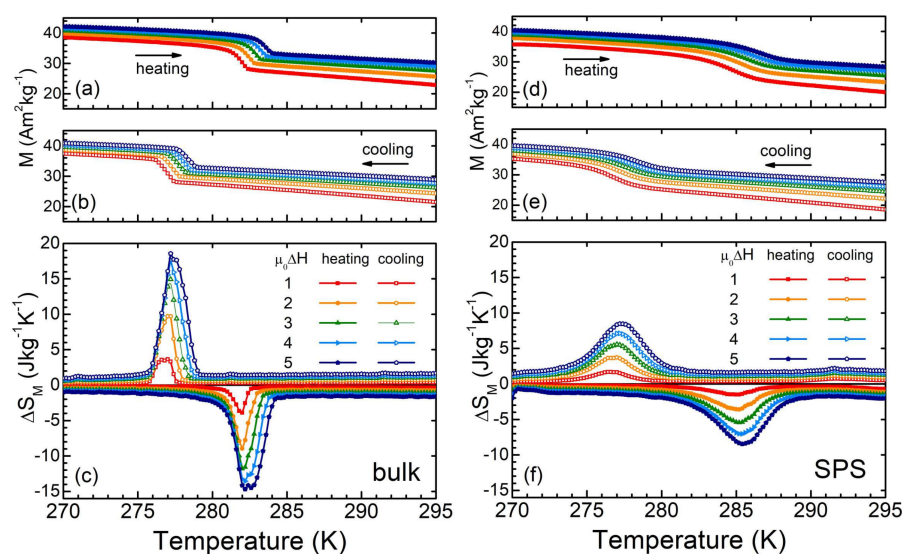


Figure 5. Left and right columns present results for bulk and SPS samples, respectively. The sections (a,b) and (d,e) show the isofield $M(T)$ curves under fields from 1 to 5 T measured across the reverse and direct MT, respectively. The sections (c,f) show the $\Delta S_M(T)$ curves through the magnetostructural transition in both directions.

Table 2. Magnetocaloric properties for a magnetic field change $\mu_0\Delta H_{\max} = 5 \text{ T}$ for bulk arc-melted and SPS samples through direct and reverse martensitic transformation.

Sample	Structural Transition	$ \Delta S_M ^{\max}$ ($\text{Jkg}^{-1}\text{K}^{-1}$)	δT_{FWHM} (K)	RCP (Jkg^{-1})
Bulk	Direct MT	18.6	2.0	28
	Inverse MT	14.7	2.2	
SPS	Direct MT	8.5	4.0	28
	Inverse MT	8.5	4.4	

To characterize the eC effect, direct measurements of $\Delta T_{\text{ad}}^{\text{me}}$ were performed through successive loading and unloading cycles of uniaxial compressive stress σ . Figure 6a shows the time dependence of $\Delta T_{\text{ad}}^{\text{me}}$ at 297 K with a loading and unloading stress of 120 MPa. Figure 6b displays the adiabatic temperature change dependence on temperature, i.e., the $\Delta T_{\text{ad}}^{\text{me}}(T)$ curves determined for both samples loading/unloading an uniaxial strain of 120 MPa. The bulk sample exhibits a $|\Delta T_{\text{ad}}^{\text{me}}|^{\max}$ of 2.4 K after stress removal, whereas this magnitude significantly decreases to 0.8 K in the SPS sample. This result agrees with the near-to-one-third reduction of the eC effect reported between the directions (100) and

(110) for two MSMA, such as a single crystal of $\text{Ni}_{50}\text{Fe}_{19}\text{Ga}_{27}\text{Co}_4$ [32] and a partially textured polycrystalline arc-melted $\text{Ni}_{50}\text{Mn}_{32}\text{In}_{16}\text{Cr}_2$ alloy [33]. A remarkable texture-induced enhancement of the elastocaloric effect was also recently reported for the Mn-rich polycrystalline $\text{Ni}_{44}\text{Mn}_{46}\text{Sn}_{10}$ alloy obtained by directional solidification [34]. Hence, for the magnetocaloric effect, the above-mentioned partial crystallographic texture explains the superior eC effect that the bulk arc-melted sample shows. The observed result also agrees with the fact that in these alloys, the Schmid factor to produce shear is larger in the (100) direction than in the (110) direction. Since the martensite phase is easier to induce in the (100) direction, the $\Delta T_{\text{ad}}^{\text{me}}(T)$ curves for the bulk arc-melted sample are broader than those of the SPS sample (35 K versus 5 K). The relationship between the $|\Delta T_{\text{ad}}^{\text{me}}|^{\text{max}}$ and the magnitude of the applied stress $\Delta\sigma$, i.e., $|\Delta T_{\text{ad}}^{\text{me}}|^{\text{max}}/\Delta\sigma$ ratio obtained for the bulk and SPS samples are 21 kGPa^{-1} and 7 kGPa^{-1} , respectively. For the bulk sample, it is comparable with the value reported in other polycrystalline alloys [14]. The $\Delta T_{\text{ad}}^{\text{me}}/\Delta\sigma$ ratio in the SPS sample is also compatible with that measured in a Ni-Fe-Ga-Co (011)-oriented single crystal [35].

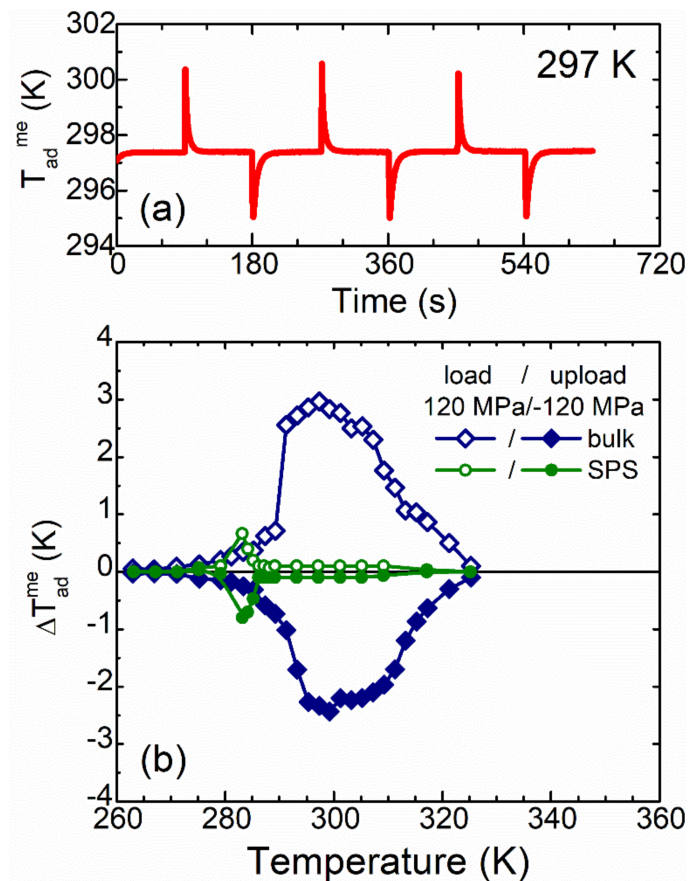


Figure 6. $\Delta T_{\text{ad}}^{\text{me}}$ as a function of time at 297 K for the bulk sample (a) and $\Delta T_{\text{ad}}^{\text{me}}(T)$ for both samples under loaded and unload applied stress of 120 MPa (b).

4. Conclusions

In summary, from the study carried out on the structural, microstructural, and phase transition characteristics, as well as the magnetocaloric and elastocaloric effects linked to the martensitic-like transformation in bulk samples of the magnetic-shaped memory alloy $\text{Ni}_{55}\text{Fe}_{11}\text{Mn}_7\text{Ga}_{27}$ produced by arc melting and spark plasma sintering, the following was demonstrated: (a) the effectiveness of the spark plasma sintering technique at consolidating highly dense polycrystalline samples of (Ni-Fe-Ga)-based alloys without showing significant changes in phase transformation temperature or in crystal structure and displaying similar MC properties compared with those obtained from the bulk sample. As far as

we know, this is the first report about the consolidation of these alloys by means of this processing technique; (b) the significant role of crystallographic texture in the enhancement of elastocaloric responses linked to the first-order structural transformation in Mn-doped (Ni-Fe-Ga)-based alloys.

Supplementary Materials: The following supporting information can be downloaded at: <https://www.mdpi.com/article/10.3390/met12020273/s1>, Figure S1: Rietveld refinement of the X-ray powder diffraction pattern of a finely pulverized sample piece taken from the bulk arc melted sample. The black open circles and red solid line represent the experimental points and Rietveld refined data, respectively, whereas the difference between experimental and simulated patterns is given by the blue line depicted at the bottom of the figure. The R-factor values obtained for the refinement were: $R_p = 11.25\%$, $R_{wp} = 28.12\%$ and $R_{exp} = 2.38\%$.

Author Contributions: Conceptualization, H.F.-Z. and J.P.C.-G.; software, J.D.N.-G. and J.P.C.-G.; validation, F.A.-H., H.F.-Z. and J.L.S.L.; formal analysis, F.A.-H.; investigation, J.D.N.-G., J.P.C.-G. and J.L.S.L.; writing—original draft preparation, J.D.N.-G. and J.P.C.-G.; writing—review and editing, J.L.S.L.; supervision, J.L.S.L., H.F.-Z. and J.P.C.-G. All authors have read and agreed to the published version of the manuscript.

Funding: This research was funded by SEP-CONACyT, grant number A1-S-37066. J.D. Navarro-García and J.P. Camarillo-García are grateful to CONACyT-Mexico for supporting their Ph.D. studies at IPICYT and postdoctoral position at UAZ, respectively.

Data Availability Statement: The data that supports the findings of this study are available within the article.

Acknowledgments: This work was supported by SEP-CONACyT, Mexico (under the research project A1-S-37066) and Laboratorio Nacional de Nanociencias y Nanotecnología (LINAN, IPICYT), where most of the experimental work was carried out. The authors are grateful to B. A. Rivera Escoto and A.I. Peña Maldonado for their technical support. J.D. Navarro-García and J.P. Camarillo-García are grateful to CONACyT-Mexico for supporting their Ph.D. studies at IPICYT and postdoctoral position at UAZ, respectively.

Conflicts of Interest: The authors declare that they have no known competing financial interests or personal relationships that could have appeared to influence the work reported in this paper.

References

1. Mañosa, L.; Planes, A. Materials with giant mechanocaloric effects: Cooling by strength. *Adv. Mater.* **2017**, *29*, 1603607. [[CrossRef](#)] [[PubMed](#)]
2. Castillo-Villa, P.O.; Soto-Parra, D.E.; Matutes-Aquino, J.A.; Ochoa-Gamboa, R.A.; Planes, A.; Mañosa, L.; González-Alonso, D.; Stipich, M.; Romero, R.; Ríos-Jara, D.; et al. Caloric effects induced by magnetic and mechanical fields in a $\text{Ni}_{50}\text{Mn}_{25-x}\text{Ga}_{25}\text{Co}_x$ magnetic shape memory alloy. *Phys. Rev. B* **2011**, *83*, 174109. [[CrossRef](#)]
3. Li, Y.; Zhao, D.; Liu, J. Giant and reversible room-temperature elastocaloric effect in a single-crystalline Ni-Fe-Ga magnetic shape memory alloy. *Sci. Rep.* **2016**, *6*, 25500. [[CrossRef](#)]
4. Bonnot, E.; Romero, R.; Mañosa, L.; Vives, E.; Planes, A. Elastocaloric effect associated with the martensitic transition in shape-memory alloys. *Phys. Rev. Lett.* **2008**, *100*, 125901. [[CrossRef](#)] [[PubMed](#)]
5. Yan, H.-L.; Wang, L.-D.; Liu, H.X.; Huang, X.M.; Jia, N.; Li, Z.B.; Yang, B.; Zhang, Y.D.; Esling, C.; Zhao, X.; et al. Giant elastocaloric effect and exceptional mechanical properties in an all-d-metal Ni-Mn-Ti alloy: Experimental and ab-initio studies. *Mater. Des.* **2019**, *184*, 108180. [[CrossRef](#)]
6. Chauhan, A.; Patel, S.; Vaish, R.; Bowen, C.R. A review and analysis of the elasto-caloric effect for solid-state refrigeration devices: Challenges and opportunities. *MRS Energy Sustain.* **2015**, *2*, E16. [[CrossRef](#)]
7. Franco, V.; Blázquez, J.S.; Ipus, J.J.; Law, J.Y.; Moreno-Ramírez, L.M.; Conde, A. Magnetocaloric effect: From materials research to refrigeration devices. *Prog. Mater. Sci.* **2018**, *93*, 112–232. [[CrossRef](#)]
8. Castillo-Villa, P.O.; Mañosa, L.; Planes, A.; Soto-Parra, D.E.; Sánchez-Llamazares, J.L.; Flores-Zúñiga, H.; Frontera, C. Elastocaloric and magnetocaloric effects in Ni-Mn-Sn(Cu) shape-memory alloy. *J. Appl. Phys.* **2013**, *113*, 053506. [[CrossRef](#)]
9. Mañosa, L.; Planes, A. Mechanocaloric effects in shape memory alloys. *Philos. Trans. R. Soc. A* **2016**, *374*, 20150310. [[CrossRef](#)] [[PubMed](#)]
10. Oikawa, K.; Omori, T.; Sutou, Y.; Morito, H.; Kainuma, R.; Ishida, K. Phase equilibria and phase transition of the Ni-Fe-Ga ferromagnetic shape memory alloy System. *Metall. Mater. Trans. A* **2007**, *38*, 767–776. [[CrossRef](#)]

11. Omori, T.; Kamiya, N.; Sutou, Y.; Oikawa, K.; Kainuma, R.; Ishida, K. Phase transformations in Ni-Ga-Fe ferromagnetic shape memory alloys. *Mater. Sci. Eng. A* **2004**, *378*, 403–408. [[CrossRef](#)]
12. Li, J.Q.; Liu, Z.H.; Yu, H.C.; Zhang, M.; Zhou, Y.Q.; Wu, G.H. Martensitic transition and structural modulations in the Heusler alloy Ni₂FeGa. *Solid State Commun.* **2003**, *126*, 323–327. [[CrossRef](#)]
13. Jiang, C.; Muhammad, Y.; Deng, L.; Wu, W.; Xu, H. Composition dependence on the martensitic structures of the Mn-rich NiMnGa alloys. *Acta Mater.* **2004**, *52*, 2779–2785. [[CrossRef](#)]
14. Xu, Y.; Lu, B.; Sun, W.; Yan, A.; Liu, J. Large and reversible elastocaloric effect in dual-phase Ni₅₄Fe₁₉Ga₂₇ superelastic alloys. *Appl. Phys. Lett.* **2015**, *106*, 201903. [[CrossRef](#)]
15. Sarkar, S.K.; Biswas, A.; Babu, P.D.; Kaushik, S.D.; Srivastava, A.; Siruguri, V.; Krishnan, M. Effect of partial substitution of Fe by Mn in Ni₅₅Fe₁₉Ga₂₆ on its microstructure and magnetic properties. *J. Alloys Compd.* **2014**, *586*, 515–523. [[CrossRef](#)]
16. Yu, H.J.; Zu, X.T.; Fu, H.; Zhang, X.Y.; Wang, Z.G. Effect of annealing and heating/cooling rate on the transformation temperatures of NiFeGa alloy. *J. Alloys Compd.* **2009**, *470*, 237–240. [[CrossRef](#)]
17. Tian, X.H.; Sui, J.H.; Zhang, X.; Zheng, X.H.; Cai, W. Grain size effect on martensitic transformation. mechanical and magnetic properties of Ni-Mn-Ga alloy fabricated by spark plasma sintering. *J. Alloys Compd.* **2012**, *514*, 210–213. [[CrossRef](#)]
18. Bai, J.; Liu, D.; Gu, J.; Jiang, X.; Liang, X.; Zhang, Y.; Zhao, X. Excellent mechanical properties and large magnetocaloric effect of spark plasma sintered Ni-Mn-In-Co alloy. *J. Mater. Sci. Technol.* **2021**, *74*, 46–51. [[CrossRef](#)]
19. Imam, H.; Zhang, H.G.; Chen, J.; Yue, M.; Lu, Q.M.; Zhang, D.T.; Liu, W.Q. Powdering and SPS sintering effect on the magnetocaloric properties of MnNiSi-based compounds. *AIP Adv.* **2019**, *9*, 035205. [[CrossRef](#)]
20. Kuang, Y.; Ai, Z.; Yang, B.; Hao, X.; Li, Z.; Yan, H.; Zhang, Y.; Esling, C.; Zhao, X.; Zuo, L. Simultaneously achieved good mechanical properties and large magnetocaloric effect in spark plasma sintered Ni-Mn-In alloys. *Intermetallics* **2020**, *124*, 106868. [[CrossRef](#)]
21. Ito, K.; Ito, W.; Umetsu, R.Y.; Tajima, S.; Kawaura, H.; Kainuma, R.; Ishida, K. Metamagnetic shape memory effect in polycrystalline NiCoMnSn alloy fabricated by spark plasma sintering. *Scr. Mater.* **2009**, *61*, 504–507. [[CrossRef](#)]
22. Li, Y.; Jiang, C.; Liang, T.; Ma, Y.; Xu, H. Martensitic transformation and magnetization of Ni-Fe-Ga ferromagnetic shape memory alloys. *Scr. Mater.* **2003**, *48*, 1255–1258. [[CrossRef](#)]
23. Barandiarán, J.M.; Gutiérrez, J.; Lázpita, P.; Chernenko, V.A.; Seguí, C.; Pons, J.; Cesari, E.; Oikawa, K.; Kanomata, T. Martensitic transformation in Ni-Fe-Ga alloys. *Mater. Sci. Eng. A* **2008**, *478*, 125–129. [[CrossRef](#)]
24. Kustov, S.; Corró, M.; Cesari, E. Stress-induced magnetization in polycrystalline Ni-Fe-Ga ferromagnetic shape memory alloy. *Appl. Phys. Lett.* **2007**, *91*, 141907. [[CrossRef](#)]
25. Pérez-Landazábal, J.I.; Recarte, V.; Gómez-Polo, C.; Seguí, C.; Cesari, E.; Dutkiewicz, J. Magnetic behavior in Ni-Fe-Ga martensitic phase. *Mater. Sci. Eng. A* **2008**, *481–482*, 318–321. [[CrossRef](#)]
26. Liu, Z.H.; Liu, H.; Zhang, X.X.; Zhang, M.; Dai, X.F.; Hu, H.N.; Chen, J.L.; Wu, G.H. Martensitic transformation and magnetic properties of Heusler alloy Ni-Fe-Ga ribbon. *Phys. Lett. A* **2004**, *329*, 214–220. [[CrossRef](#)]
27. Recarte, V.; Pérez-Landazábal, J.I.; Gómez-Polo, C.; Cesari, E.; Dutkiewicz, J. Magnetocaloric effect in Ni-Fe-Ga shape memory alloys. *Appl. Phys. Lett.* **2006**, *88*, 132503. [[CrossRef](#)]
28. Bruno, N.M.; Karaman, I.; Chumlyakov, Y.I. Orientation dependence of the elastocaloric effect in Ni₅₄Fe₁₉Ga₂₇ ferromagnetic shape memory alloy. *Phys. Status Solidi B* **2018**, *255*, 1700437. [[CrossRef](#)]
29. Guillon, O.; Gonzalez-Julian, J.; Dargatz, B.; Kessel, T.; Schierning, G.; Räthel, J.; Herrmann, M. Field-assisted sintering technology/spark plasma sintering: Mechanisms, materials, and technology developments. *Adv. Eng. Mater.* **2014**, *16*, 830–849. [[CrossRef](#)]
30. Bruno, N.M. The Magnetocaloric and Elastocaloric Effects in Magnetic Shape Memory Alloys. Ph.D. Thesis, Texas A&M University, College Station, TX, USA, 2015.
31. Marcos, J.; Planes, A.; Mañosa, L. Magnetic field induced entropy change and magnetoelasticity in Ni-Mn-Ga alloys. *Phys. Rev. B* **2002**, *66*, 224413. [[CrossRef](#)]
32. Xiao, F.; Jin, M.; Liu, J.; Jin, X. Elastocaloric effect in Ni₅₀Fe₁₉Ga₂₇Co₄ single crystals. *Acta Mater.* **2015**, *96*, 292–300. [[CrossRef](#)]
33. Henández-Navarro, F.; Camarillo-García, J.P.; Aguilar-Ortiz, C.O.; Flores-Zúñiga, H.; Ríos, D.; González, J.G.; Álvarez-Alonso, P. The influence of texture on the reversible elastocaloric effect of a polycrystalline Ni₅₀Mn₃₂In₁₆Cr₂ alloy. *Appl. Phys. Lett.* **2018**, *112*, 164101. [[CrossRef](#)]
34. Zhang, G.; Li, Z.; Yang, J.; Yang, B.; Wang, D.; Zhang, Y.; Esling, C.; Hou, L.; Li, X.; Zhao, X.; et al. Giant elastocaloric effect in a Mn-rich Ni₄₄Mn₄₆Sn₁₀ directionally solidified alloy. *Appl. Phys. Lett.* **2020**, *116*, 023902. [[CrossRef](#)]
35. Zhao, D.; Xiao, F.; Nie, Z.; Cong, D.; Sun, W.; Liu, J. Burst-like superelasticity and elastocaloric effect in [011] oriented Ni₅₀Fe₁₉Ga₂₇Co₄ single crystals. *Scr. Mater.* **2018**, *149*, 6–10. [[CrossRef](#)]